ELSEVIER

Polymer 41 (2000) 2271–2288

polymer

Changes in the morphology and orientation of bulk spherulitic polypropylene due to plane-strain compression

M. Pluta*, Z. Bartczak, A. Galeski

Centre of Molecular and Macromolecular Studies, Polish Academy of Sciences, Sienkiewicza 112, 90-363 Lodz, Poland

Received 17 November 1998; received in revised form 16 April 1999; accepted 14 May 1999

Abstract

Studies on the morphology and the development of texture in isotactic polypropylene (iPP) subjected to plane-strain compression are reported. The iPP samples were compressed in a channel-die at 110°C up to the true strain of 1.89 (compression ratio, CR = 6.6). The structure of deformed specimens was investigated by means of light microscopy, differential scanning calorimetry, density measurements, small- and wide-angle X-ray diffraction techniques and dynamic mechanical analysis. A scheme of morphology changes on all structural levels was proposed. It was found that initial spherulitic morphology was destroyed and was transformed into stacks of crystalline lamellae with their normals rotating towards loading direction, while chain axis tending towards the flow direction at the true strain near 1.1 (CR ≈ 3). The main active deformation mechanisms found were the crystallographic slips along the chain direction: (010)[001], (110)[001] and (100)[001] slip systems, supported by the deformation of the amorphous component by interlamellar shear. No evidence of the twinning modes was found. The intense chain slip caused the fragmentation of the lamellae into smaller crystalline blocks due to slip instabilities. That transformation occurred above true strain of 1.39 (CR = 4). Further slips in these fragmented crystallites led to formation of a sharp orientation of the chains along the flow direction. The final texture of the compressed iPP found at the true strain of 1.89 (CR = 6.6) was the multi-component texture with two main components of (010)[001] and (110)[001]. Mechanical properties of deformed samples follow the evolution of their structure through successive increase of storage modulus and a decrease of mechanical loss, ascribed to the glass–rubber transition, with increasing strain. The behavior of mechanical loss evidences substantial stiffening of the amorphous component with increasing strain. © 1999 Elsevier Science Ltd. All rights reserved.

Keywords: Polypropylene; Plastic deformation; Compression

1. Introduction

The plastic deformation and the resulting orientation of semi-crystalline polymers is of great importance for many technological processes such as fibre drawing, biaxial stretching of films, solid-state processing, etc. Due to unquestionable practical as well as scientific interests, the plastic deformation of various semicrystalline polymers, including isotactic polypropylene, has been widely and intensively studied over the last three decades (see e.g. [1–4]). These studies demonstrated that in the plastic deformation process of this class of polymers several deformation mechanisms of crystallographic nature are involved. These mechanisms are in general analogous to those found in deformation of metals and other low molecular crystalline materials. There are, however, some additional phenomena specific for polymers, like the structural transformation from lamellar to microfibrillar structure occurring upon drawing, not observed in deformation of low-molecular mass materials. The currently accepted mechanism of that transformation is '*micronecking*' due to Peterlin [5], although recent studies of deformation of polyethylene [6,7] demonstrated that simultaneous action of several crystallographic mechanisms supported by deformation of amorphous component like interlamellar shear are sufficient for a continuos transformation of a semicrystalline polymer from initial spherulitic morphology to the final highly textured material. These studies show that cavitation, essential for micronecking model, seems to be only a side effect which obscures the crystrallographic mechanisms underlying the phenomena of plastic deformation of semicrystalline polymers.

The aim of present study was to investigate the orientation behavior and mechanisms involved in the plastic deformation of bulk isotactic polypropylene (iPP) with initial spherulitic morphology by plane-strain compression using a channel-die. Many detailed orientation studies have been carried out on this commercially important polymer,

---

* Corresponding author.

PII: S0032-3861(99)00364-X

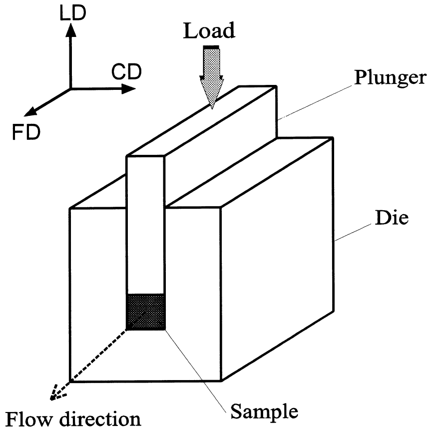

Fig. 1. Diagram of compression in a channel-die.

deformed by uniaxial drawing (e.g. [8–10]), biaxial drawing [11–13], uniaxial compression [14–20], rolling [21–24], die drawing [25,26], solid-state extrusion [27–29] or combined methods. However, still relatively little is known about the plastic deformation mechanisms involved, mostly due to complicated morphology of iPP. The plane-strain compression in a channel-die was chosen as a deformation method since relatively simple strain field is produced. This makes interpretation of the results simpler than in cases of other deformation modes. Moreover, the compressive stresses, which are generated during deformation process prevent cavitation phenomena frequently associated with other deformation modes. Last, the channel-die compression proceeds homogeneously over the entire sample volume, without any instabilities such as necking observed on drawing. This allowed us to probe the morphology and crystalline texture evolution of the material in a wide range of plastic strain.

2. Experimental

2.1. Samples preparation and orientation

Isotactic polypropylene (iPP) used in this work was Malen-P B200 (Petrochemia SA., Poland; melt flow index of 0.6 g/10 min [2.16 kG at 230°C], density 0.91 g/cm^3). Virgin iPP pellets were extruded into profiles of rectangular cross-section of 12×52 mm^2. The rate of extrusion, 5 mm/min, was slow enough for solidification of the extruded iPP melt inside the long forming-die. The profiles produced had negligibly small orientation (verified by X-ray diffraction), spherulitic morphology of the core, and contained no voids or bubbles, frequently present in compression moulded thick polymer plates. Rectangular shaped specimens for deformation study were cut out from the extruded profiles and the skin layer was removed by careful machining. The sizes of the specimens after machining were: 10 mm wide, 50 mm long and up to 60 mm high, depending on the plastic strain targeted. The surfaces of the specimens were polished.

The specimens were subjected to plane-strain compression in a channel-die, shown schematically in Fig. 1. This method of deformation was described in detail elsewhere [6,30]. Prior to tests the specimen surfaces were lightly lubricated with a molybdenum grease to reduce friction against the plunger and the walls of the channel-die. Next, the specimen was placed inside a channel-die assembly and heated up to temperature desired for deformation experiment. The Instron Testing Machine model 1113 of the capacity of 50 kN was used as a loading frame. The deformation was performed at 110°C and the crosshead speed was adjusted to the actual sample height in order to obtain an initial deformation rate of approximately 0.5% per min. The load and plunger displacement were measured during the compression test. The compression was stopped after reaching of desired compression ratio (CR). The sample was then allowed to cool down, still under load. Load was released at room temperature, usually 4 h after completion of deformation. The samples with the following CRs of 1.54, 2.1, 2.4, 3.0, 4.0, 5.7, 6.6 were prepared.

2.2. Density measurements

Density of the samples was measured in a 1 m high gradient column filled with a mixture of ethyl alcohol and water and calibrated with glass beads of various density within the column range. The temperature of the column was maintained at 22 ± 0.2°C.

2.3. Differential scanning calorimetry

The melting behavior of the deformed samples was characterized using a DuPont TA 2000 differential scanning calorimeter (DSC). The 5–8 mg specimens were cut out from deformed samples in plane perpendicular to the flow direction. As a reference the sample of unoriented iPP with similar thermal history was also investigated. The DSC scans were made with a heating rate of 10°C/min.

2.4. Light microscopy

The morphology of the compressed samples was examined by means of optical microscope with polarized light. The 5 μm thick sections for microscopical observations were cut in planes perpendicular to the loading or constraint direction, LD and CD, respectively (for explanation of sample axes, see Fig. 1). The sections of undeformed sample were also examined. The sections were cut at room temperature using TESLA BS 490A ultramicrotome equipped with glass knives.

2.5. Viscoelastic measurements

The dynamical mechanical properties of the deformed samples were measured using a Dynamic Mechanical Thermal Analyzer Mk III (Rheometric Scientific) in a single cantilever bending mode. The specimens in the form of 15 mm long, 10 mm wide and 1 mm thick bars were machined out of deformed samples parallel to the flow direction. The gauge length was 5 mm. The storage modulus, E', and loss factor, tan δ, were measured at a constant frequency of 1 Hz as a function of temperature varied within the range from -100 to 150°C with a heating rate of 2°C/min.

2.6. Small-angle X-ray scattering

The evolution of the lamellar structure in the deformed samples was probed with small-angle X-ray scattering (SAXS). The specimens approximately 1 mm thick were carefully machined out from the deformed samples in planes perpendicular to the loading (LD), constraint (CD) or flow (FD) direction. The 2D SAXS patterns were recorded using a Siemens Hi-Star area detector, controlled by a GADDS software, coupled to an 18 kW rotating anode X-ray generator (Cu Kα radiation; Rigaku RV-300). The pinhole collimator system provided a point focus with a beam diameter of approximately 0.5 mm. The distance between a sample and the detector was chosen to be 1250 mm and the recording time was fixed at 3 h. Standard procedures were used for the correction of the detector sensitivity, primary beam profile and background scattering.

2.7. X-ray diffraction

The orientation of the crystallographic planes of iPP crystallites in the deformed samples was examined by means of an automated computer-controlled wide-angle X-ray diffractometer system (WAXS) consisting of a pole figure device associated with a wide-angle goniometer coupled to sealed-anode X-ray generator operating at 30 kV and 30 mA (Cu Kα radiation; DRON, Russia). The complete pole figures were obtained for the projections of Euler angles of sample orientation with respect to the incident beam, α varying from 0 to 90° in 5° intervals and β varying from 0 to 360° in 5° steps. The construction of complete pole figures required the connection of the X-ray data collected in both transmission and reflection modes. The connection angle was $\alpha_c = 50°$, i.e. the reflection mode was used for $\alpha = 0$–50°, and the transmission mode for $\alpha = 50$–90°. The following diffraction reflections from crystals of monoclinic modification of iPP were analyzed: (110), (040), (130), (060) and $(\bar{1}13)$ (diffraction angle $2\Theta \approx 14.1$, 16.9, 18.5, 25.5 and 42.5°, respectively). The slit system of the diffractometer was adjusted to measure the integral intensity of the appropriate diffraction peak. The necessary corrections for background scattering and sample absorption were introduced. The diffraction data were further corrected for the X-ray beam defocusing due to sample tilt and other instrumental effects using the data obtained at identical experimental conditions for random (unoriented) standard specimen of iPP of the same thickness as the measured deformed samples [31]. The pole figure plots were generated by the program POD, a part of the popLA package (Los Alamos National Laboratory, Los Alamos, NM, USA). All figures were plotted in a stereographic projection with linear intensity scale. Prior to plotting the calculated pole densities were self-normalized to the random pole distribution and then plotted in the units of multiplication of a density of random distribution (m.r.d. units; 1 is equal to the density of random distribution).

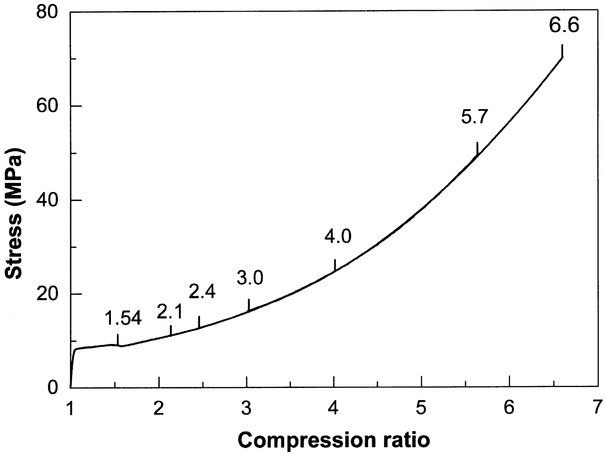

Fig. 2. Exemplary stress–CR curve for a polypropylene sample compressed in a channel-die at 110°C with the deformation rate of 0.5% per min.

3. Results and discussion

3.1. Mechanical response on compression

A typical stress vs. CR dependence for the iPP material deformed in a channel-die at 110°C is shown in Fig. 2. The marks on the curve correspond to the individual specimens deformed to the CR indicated and then taken for further investigations. Since the cross-section of the sample deformed in a channel-die remains constant in the course of the entire deformation process the stress represented in Fig. 2 is equivalent to the true stress. The CR can be easily recalculated to the true strain e through the relation $e = \ln(\mathrm{CR})$ [1].

Fig. 2 shows that the stress–strain curve for iPP is similar to the respective curves obtained for other polymers compressed in plane-strain compression, e.g. linear polyethylene [6] or nylon-6 [32]. The process of plastic deformation and the plastic flow characterized by plateau on the stress–CR curve occurs in the range of CR from 1.07 to 1.8. Above CR of 1.8 a significant strain hardening develops. At CR of 6.6 (true strain of 1.89) the stress reaches the value of nearly 70 MPa (at compression temperature of 110°C). Similarly to PE compressed in a channel-die [6], the deformation of iPP is permanent in the entire strain range studied the specimens exhibited very small (less than 1%) plastic strain recovery on unloading at room temperature.

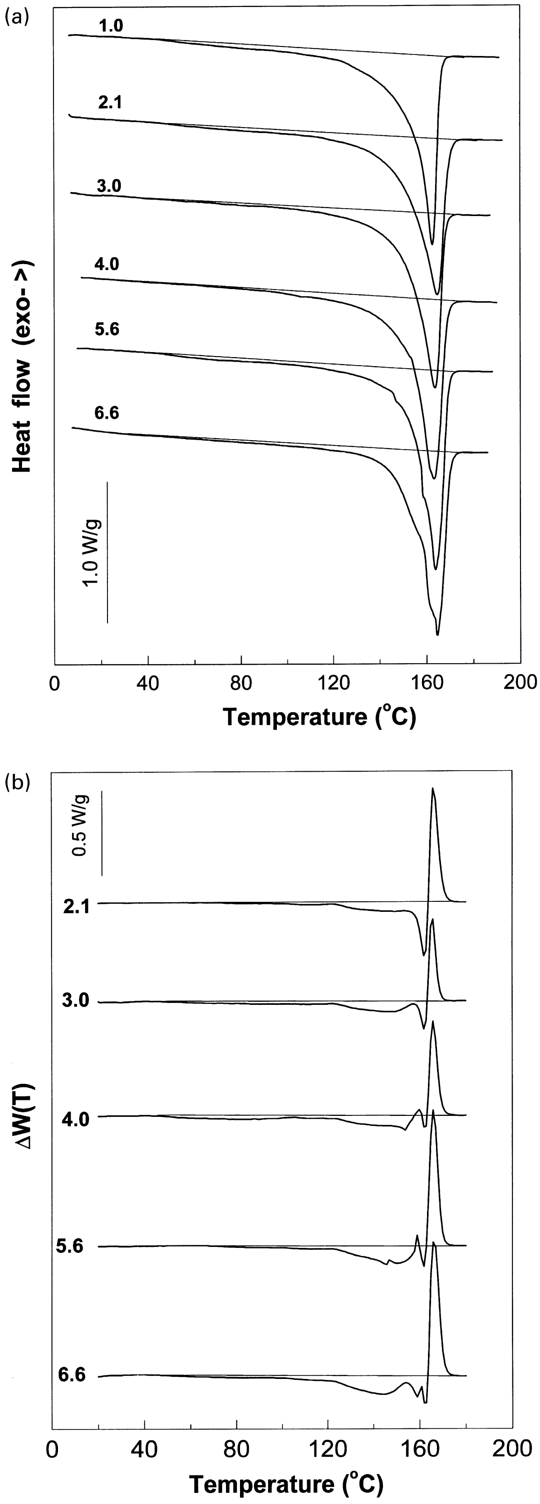

Fig. 3. DSC thermograms for the undeformed and deformed samples of iPP obtained on heating with the rate of 10°C/min. (a) The curves are normalized to the unit mass of the sample and (b) the difference curves obtained by subtracting of the curve of undeformed sample from these of the deformed samples.

3.2. Thermal properties and crystallinity

Fig. 3(a) presents the DSC melting thermograms of the samples deformed to various CRs, indicated in the figure. For reference the thermogram of a sample of undeformed iPP, but of identical thermal history as deformed samples is also shown. The slight fluctuations seen on the DSC traces of samples of higher CR at temperature range from 140 to 160°C result from the change of thermal contact between sample and the pan due to sample shrinkage on heating above the temperature of deformation.

The DSC thermograms show characteristic melting behavior of monoclinic crystals of iPP with a single peak at the range of 162–165°C. The presence of monoclinic form only in the samples studied was confirmed independently by the X-ray diffraction measurements. In unoriented sample in addition to a main peak at 163.3°C related to the melting process of stable monoclinic form the undeformed sample exhibits a weak endothermic shoulder in a low temperature range, with onset at about 40°C. This endotherm can be attributed to the thermal destruction of small sized crystallites or less ordered phase. In the case of the deformed samples the area of the low temperature shoulder is smaller and the main melting peak is shifted towards slightly higher temperatures as compared to undeformed reference sample. The enthalpy of melting, and calculated crystallinity degree of compressed samples decrease with an increasing strain. Calorimetric parameters determined from the thermograms, i.e. the temperature of the melting peak, T_m, the heat of fusion, ΔH, and the calculated degree of crystallinity, X_c are collected in Table 1. For the calculation of X_c the heat of fusion of crystalline phase of iPP of 209 J/g was assumed [33].

To get more information on the influence of deformation on the thermal behavior the DSC curves from Fig. 3(a) were replotted in Fig. 3(b) in the form of differential curves, $\Delta W(T)$, calculated according to the formula:

$$\Delta W(T) = W(T)_{\mathrm{d}} - W(T)_{\mathrm{un}}$$

where $W_{\mathrm{d}}(T)$ and $W_{\mathrm{un}}(T)$ are the values of the heat flow measured at a given temperature T for deformed and undeformed specimens, respectively. The difference curves are negative in the range of temperatures below 163°C, and positive above it. Below 163°C the difference rises slightly with an increasing CR. Such behavior reflects a decreasing amount of less stable or small sized crystallites in deformed samples. In contrast, the positive difference values at temperatures above 163°C indicate an increase of the fraction of crystallites of enhanced thermal stability (presumably larger thickness) in all deformed samples. The above changes are relative, not absolute, since the overall crystallinity degree decreases with increasing strain (see Table 1).

In Table 1 the density of the investigated samples is presented along with the calorimetric data. The density also decreases with an increasing strain, which corresponds to the trend observed for crystallinity determined from DSC

Table 1
Calorimetric and density data of undeformed and deformed iPP samples derived from the DSC and gradient column measurements

Compression ratio	Melting temperature (°C)[a]	Heat of fusion[b] (J/g)	Degree of crystallinity[c]	Density (g/cm^3)
1	163.5	109.9	0.526	0.9131
2.1	164.6	108.6	0.52	0.9109
3	164	104.9	0.502	0.907
4	163.9	105.7	0.506	0.9053
5.7	164	105.8	0.506	0.9031
6.6	164.6	101	0.48	0.9035

[a] Determined as the maximum of a main melting peak.
[b] Evaluated in the temperature range from 40 to 180°C.
[c] Calculated from measured heat of fusion; $\Delta H_f = 209$ J/g [33].

data. Fig. 4 shows the changes in the crystallinity degree relative to the crystallinity of a reference undeformed sample, with respect to the CR. The crystallinity, as determined independently from both density and calorimetric data, decreases with increasing CR. However, the crystallinity estimated from density decreases somewhat faster than that determined from enthalpy measurements.[1] That discrepancy in estimated changes of crystallinity might be a result of the presence of the micro-voids in deformed samples. However, possibility of cavitation during deformation is rather remote due to presence of compressive stresses generated on compression in a channel-die. Indeed, the SAXS experiments (see further sections) did not indicate any noticeable scattering characteristic for micro-voids. Therefore, the decrease of density must be attributed with another phenomena, possibly with changes within crystalline component, as formation of shear bands and/or destruction of lamellar morphology, due to plastic deformation, which led to locally less dense packing.

3.3. Dynamic mechanical properties

The temperature dependencies of the mechanical loss, tan δ, of the undeformed and deformed samples of iPP, compressed to various strain are shown in Fig. 5. All presented curves demonstrate three dynamic mechanical relaxation processes, typical for the isotactic polypropylene, labeled as: γ (around −50°C), β (around 0°C) and α (above 30°C). Analysis of the origin of these processes was the subject of numerous studies (e.g. [35–42]).

The γ-relaxation process was assigned to the local relaxation mode, involving a few chain segments of the amorphous phase. Fig. 5 shows that in the γ-relaxation region the curves of tan δ of all investigated samples exhibit weak and broad maximum, position of which is independent on CR. However, this maximum in the deformed samples is somewhat flattened as compared to the reference undeformed sample, reflecting a decrease of the intensity of the γ process. This can indicate some restriction of segmental mobility of the amorphous phase in oriented samples.

The maximum of β relaxation is the most discernible maximum for the undeformed iPP. The β relaxation process is usually attributed to the glass–rubber transition of the amorphous phase (some authors invoke a double transition involving unconstrained regions of the amorphous phase and regions constrained by crystallites [39,40]). The position of this maximum at low frequencies can be assigned to the glass transition temperature T_g. As it can be observed in Fig. 5, the peak of β relaxation decreases and shifts towards higher temperature with increasing strain, which is demonstrated by inset in Fig. 5. The area under the β peak for deformed samples, A, was determined after subtraction of fitted exponential baseline and related then to the area of respective peak determined for the undeformed reference sample, A_1. It can be seen that T_β progressively increases from 6 to 17°C, while the area of the β peak decreases nearly 10 times with an increase of CR from 1 to 6.6. Such changes of the mechanical relaxation of the β process indicate clearly a substantial reduction of mobility of the chains in the amorphous phase. As the overall crystallinity of the deformed samples is lowered only slightly as compared to

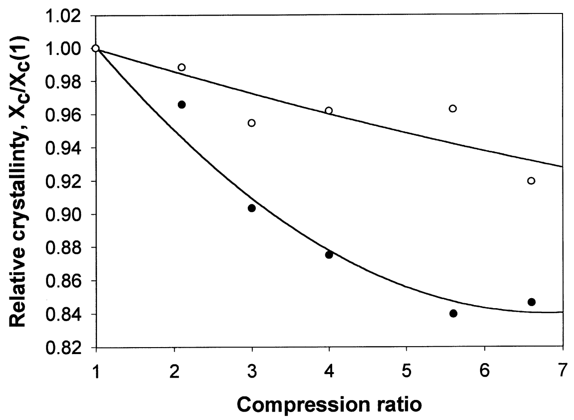

Fig. 4. The dependence of relative crystallinity of compressed samples of iPP (related to the crystallinity of the undeformed reference sample) on CR, calculated from heat of fusion (○) and density (●) data.

---

[1] The absolute values of crystallinity calculated from DSC data remain lower than those calculated from density in the entire strain range studied; they matched when $\Delta H_f = 165$ J/g [34] was used instead of 209 J/g in the calculation.

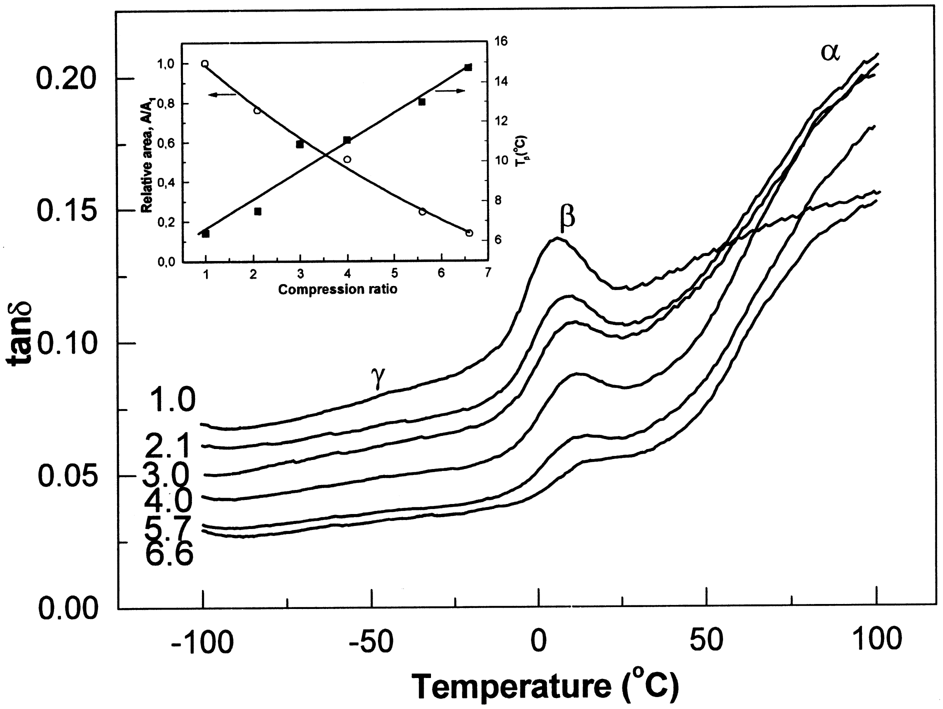

Fig. 5. The dependence of mechanical loss, tan δ (measured at 1 Hz and heating rate 2°C/min) as a function of temperature for iPP samples deformed to various CRs. The curves were shifted by the factor of 0.01 for clarity of presentation. Inset: Dependence of temperature of the β relaxation peak, T_β, and the magnitude of the β relaxation process (the ratio of the area under the tan δ peak of the deformed sample and undeformed reference sample, A/A_1).

the undeformed iPP, the observed substantial damping of the β process with increasing strain should be interpreted in terms of successive changes in molecular packing of the amorphous phase resulting in reduced mobility.

The α relaxation process manifests by an increase of the tan δ at temperatures above 30°C, with a maximum at approximately 110°C. In Fig. 5 only the low temperature component of the α process is shown, because at the temperature above 100°C the DMTA data are strongly interfered with artifacts produced by the shrinkage forces generated in oriented samples. That shrinkage is the strongest at about 120°C, i.e. above temperature of deformation, $T_d = 110$°C.

As can be observed in Fig. 5 tan δ of the undeformed sample increases gradually with temperature in the temperature range of the α relaxation. The curves of tan δ of deformed samples also rise in this range of temperature but all of them rise with the slope much larger than the slope of the curve of undeformed iPP, especially in the temperature range above 50°C. Such a behavior indicates a common mechanism of the α process in the deformed samples in spite of a successive reorganization of both amorphous and crystalline components due to plastic strain. Moreover, this can support the view that the orientation of the amorphous component produced by interlamellar shear develops fast at relatively low strain and then "saturates" and remains on that high level with further strain increase [6]. Considering above one can suppose that the low temperature part of the α process in the deformed samples is dominated by the phenomena of relaxation of orientation in the noncrystalline component in interlamellar regions probably due to activation of shrinkage phenomena.

In Fig. 6, the storage modulus E' of the investigated samples is plotted against temperature. The E' modulus is well correlated with the CR of the samples: the higher the CR the higher is E' value over the entire temperature range.

Moreover, it can be observed that with increasing temperature the value of E'

—decreases slightly in the γ relaxation region for all undeformed and deformed samples,

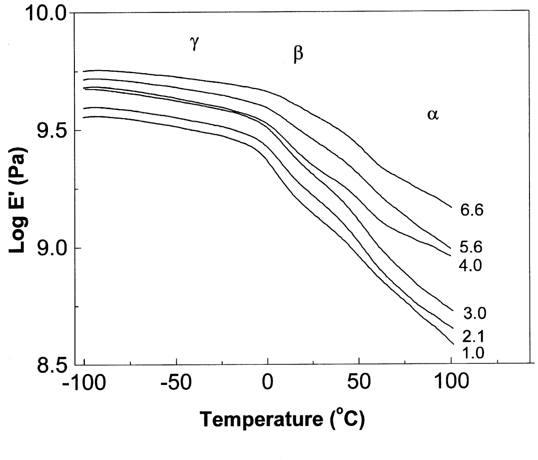

Fig. 6. Dynamic storage modulus (E') as a function of temperature for samples of iPP deformed to CR indicated for each curve.

—drops in the β relaxation region faster in samples of smaller CR. The onset of that drop of E' shifts to higher temperatures with an increasing CR and

—decreases gradually in the α relaxation region, however with a second drop at temperature around 55°C, which is accompanied by an increase of the tan δ (cf. Fig. 5).

The differences in the dynamic mechanical response of the deformed samples, especially in the β relaxation region, should be ascribed primarily to the variation in the structure of the non-crystalline component resulting from deformation-induced molecular orientation within this phase. It was demonstrated for uniaxially compressed iPP [18–20] that the density of the amorphous phase increases markedly with an increasing strain, which indicates that the average intermolecular distance is smaller than respective distance in an unoriented amorphous component. The detailed study of the orientation of amorphous component of high density polyethylene deformed by the channel-die compression [43] demonstrated that on large-scale plastic deformation the amorphous component of semi-crystalline HDPE undergoes profound transformation toward ordered structure of chains aligned along flow direction, and moreover, arranged in a 2-D pseudo-hexagonal lattice. Such ordering causes an increase of the density of non-crystalline component and should, of course, induce serious modification of its properties, including the relaxation behavior discussed above. Moreover, the reorganization of the lamellar structure occurring at higher plastic strain (see following sections) results in stronger constraints imposed on the interlamellar amorphous material which is intimately connected to the transforming crystallites. That increase of constraints will make amorphous layers stiffer than those in the undeformed sample and consequently will result in modification of the mechanical response of the oriented sample.

3.4. Morphological alterations

Figs. 7 and 8 show the polarized light micrographs of thin sections of the undeformed and deformed samples, respectively. The undeformed sample (Fig. 7(a)) exhibits a well-developed spherulitic structure with the spherulite diameter ranging from 30 to 100 μm. For the evaluation of changes in supermolecular structure of the deformed samples two sets of sections cut in planes perpendicular to the loading and constraint directions, LD and CD respectively, were investigated. When the samples are viewed from LD the spherulitic morphology can be detected in samples deformed to low and moderate strains. In the sample of the true strain of 0.74 (CR = 2.1), i.e. deformed to the initial stage of strain hardening, the spherulitic morphology can be readily identified (cf. Fig. 7(b)). The spherulites appear to be slightly elongated along the flow direction, FD. In samples of CR = 3 and 4 (Fig. 7(c)) the spherulitic structure seems to transform gradually and eventually disappear due to increasing strain, yet the elongated remnants of the single spherulites can still be recognized. For samples of higher strain no trace of the spherulitic structure is visible. Instead, in the sample with CR = 5.7 (Fig. 7(d)) and 6.6 the bright birefringent bands parallel to the FD can be observed.

Table 2
Shear bands spacing and the angle of inclination of the band to the flow direction, as determined from optical micrographs

Compression ratio	Band spacing (μm)	Inclination angle (°)
1	–	–
2.1	28	± 15
3	16.6	± 12
4	15	± 5
5.7	13.3	≈ 0
6.6	6.1	≈ 0

Micrographs of sections cut perpendicularly to CD, are shown in Fig. 8. They provide information complementary to the LD view on the deformation-induced morphology changes. In contrast to the LD view, the samples viewed in the CD direction do not show spherulitic morphology even for the relatively low true strain of 0.74 (CR = 2.1; see Fig. 8(a)). The spherulitic structure is replaced here by two sets of intersecting elongated features inclined at some acute angle towards FD. They represent microscopic shear bands produced by the plastic deformation. These bands become finer and tilted at smaller angle with respect to FD with true strain increasing to 1.1 (CR = 3) and then to 1.39 (CR = 4; see Fig. 8(b)). In the sample strained to 1.74 (CR = 5.7; Fig. 8(c)) these fine bands undergo crumbling to the shorter ones, now all oriented very close to the flow direction, FD. The sample with the highest strain 1.89 studied (CR = 6.6; Fig. 8(d)) shows a very dense collection of thin shear bands oriented entirely along FD, which gives an appearance of a layered structure. Such layered structure was also reported for iPP compressed uniaxially to the CR of 6.9 and higher [18–20].

Closer examination of the micrographs taken in CD view allowed to estimate the lateral spacings of the discussed bands and the angle of their inclination with respect to FD. These data are presented in Table 2.

The changes of morphology similar to these reported above for iPP, including formation of microscopical shear bands, were also observed in samples of HDPE [6] and nylon-6 [32], deformed by compression in a channel-die. However, in these polymers the shear bands at approximately ±45° with respect to the flow direction appeared in samples deformed above the CR of 1.6–1.8. With increasing strain these shear band multiplied in number and gradually tilted toward FD. The multiplication of the shear bands number was observed especially in compressed HDPE. The shear bands in compressed nylon-6 were formed preferentially at former spherulite boundaries, while in PE no such correlation was found. There is also no clear evidence in this study that any of the shear bands observed in iPP was formed at boundaries between spherulites.

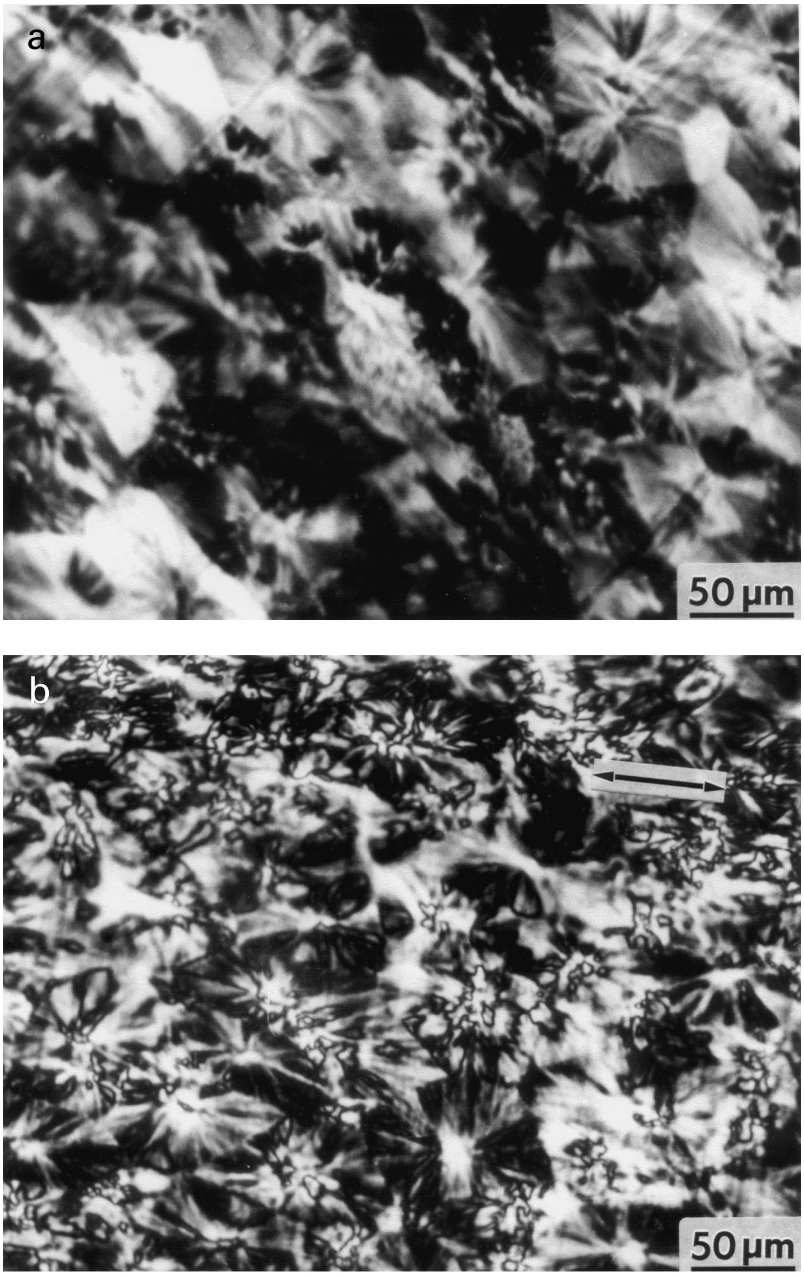

Fig. 7. Polarizing light micrographs of iPP thin sections cut perpendicular to loading direction from samples deformed in a channel die at 110°C to the CR: (a) 1, undeformed reference sample; (b) 2.1; (c) 4.0; (d) 5.7.

The initial inclination angle of the shear bands found in compressed iPP samples was only $\pm 15^\circ$ with respect to FD ($\mathrm{CR} = 2.1$), which angle is much lower than anticipated $\pm 45^\circ$, observed in HDPE or nylon. We do not have explanation for such unexpected behavior.

3.5. Evolution of the lamellar structure

The lamellar structure of the deformed iPP samples was probed with two-dimensional small angle X-ray scattering (2-D SAXS).

The 2-D SAXS pattern for the undeformed sample (not shown here) has a form of an uniform ring, which indicates a random distribution of lamellae in this initial sample exhibiting a spherulitic morphology. The long period determined for this sample was 22.3 nm. Fig. 9 presents the contour plots of the 2-D SAXS patterns obtained for the deformed samples viewed in three orthogonal directions associated with the reference axes of a channel-die: LD, CD and FD (for definition see Fig. 1). Since 2-D contour plots do not reveal enough detail, the patterns of Fig. 9 are supplemented with their sections along 2θ in two principal directions of sample orientation. These plots are presented in Fig. 10(a), (b) and (c), for LD, CD and FD illuminations,

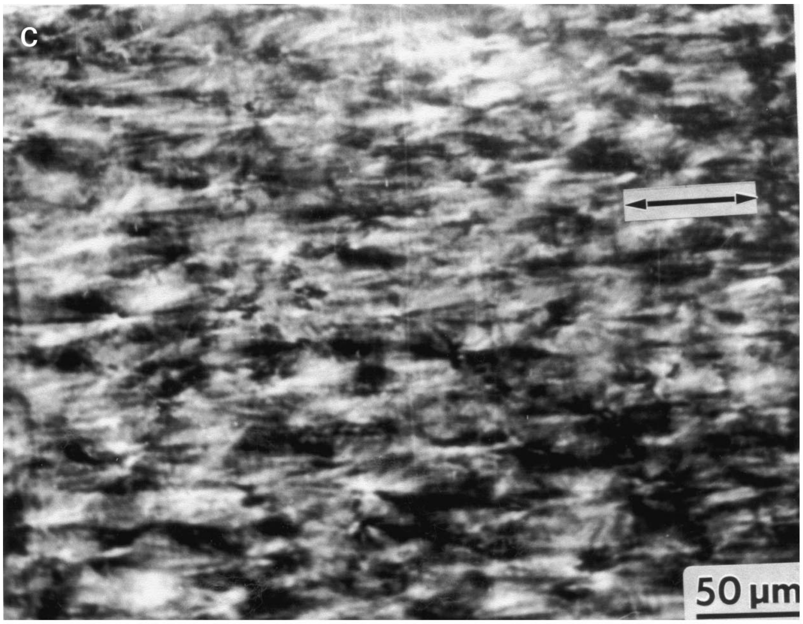

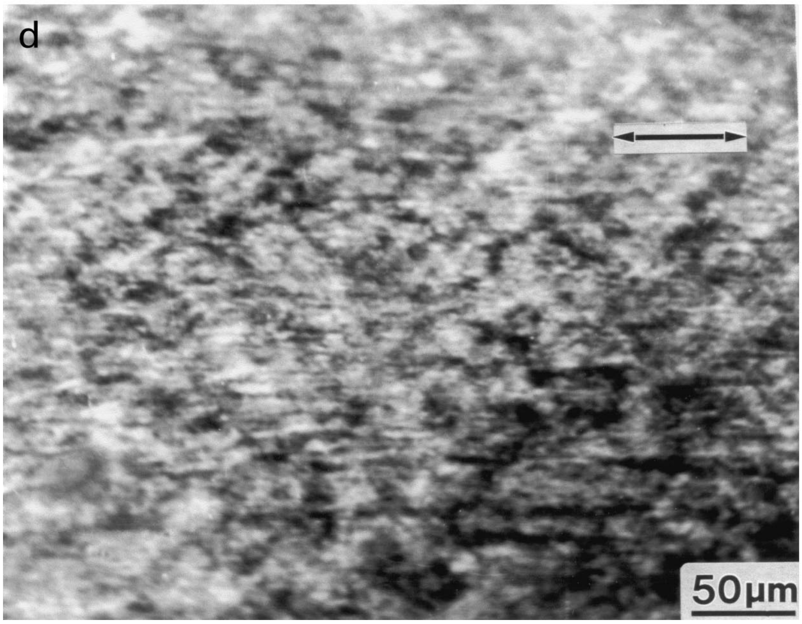

Fig. 7. (*continued*)

respectively. Additionally, in order to demonstrate the 4-point character of the 2-D SAXS patterns obtained in CD view, Fig. 11 presents the azimuthal scans of these patterns made for the range of 2θ angle within which the scattering intensify had a maximum.

The SAXS patterns recorded for deformed samples differ markedly from an uniform ring observed in the undeformed reference specimen. In the sample compressed to the CR of 2.1 and illuminated along LD that ring transforms into a 2-point pattern oriented along CD (see left column in Fig. 9 and also Fig. 10(a)). In the CD view the SAXS pattern has a clear 4-point character (center column in Fig. 9, see also Figs. 10(b) and 11). In the FD illumination the SAXS pattern has again a 2-point character, albeit it is less developed than the pattern observed for LD illumination (nearly complete scattering halo can be still recognized here with two maxima in the direction of loading, see right column in Fig. 9 and also Fig. 10(c)).

The patterns similar to these described above were observed also for the samples deformed to higher CR of 3.0 and 4.0. However, with increasing CR the intensity of the scattering gradually decreases. The angular distance between the maxima in the 4-point pattern observed in the CD-view pattern also decreases with increasing strain (from $2\psi = 37°$, as determined for CR $= 2.1$, to 14° for CR $= 4.0$; cf. Figs. 10 and 11). The long periods evaluated from the

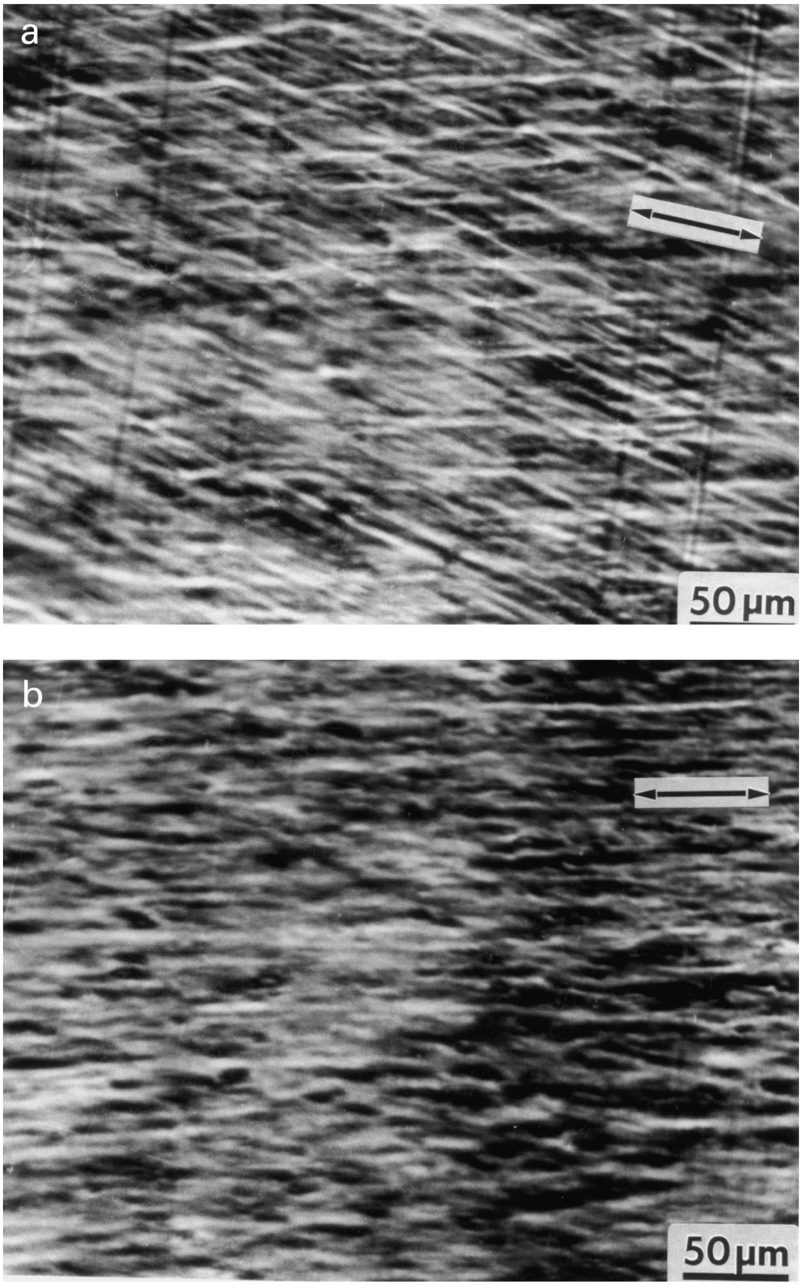

Fig. 8. Polarizing light micrographs of iPP thin sections cut perpendicular to constraint direction from samples deformed in a channel die at 110°C to the CR: (a) 2.1; (b) 4.0; (c) 5.7; (d) 6.6.

discussed patterns along FD (determined in the LD-view and CD-view patterns) and CD direction (in LD-view and FD-view patterns) remain practically constant, around 22 nm, which is close to the long period of the reference undeformed iPP. On contrary, the long period evaluated along LD (in the CD-view and FD-view patterns) decreases monotonically with increasing CR.

The 4-point SAXS pattern observed in the CD-illumination indicates the formation of two dominant population of lamellae due to plastic deformation, both oriented with their normals in the LD–FD plane and symmetric with respect to FD. The intensity of scattering maxima for this illumination mode is higher than the maxima observed in other views. This suggests that these two populations are dominant in the entire domain of lamellar orientation. The angle between normals to these lamellae and the direction of loading, decreasing with increasing strain, correlates well with the orientation angle of the intersecting microscopic shear bands observed by optical microscopy in the CD-view (cf. Figs. 11 and 4, and Table 2). Therefore, it may be inferred that these microscopic shear bands are the result of an intense plastic shear and accompanying reorientation of deformed lamellae with their surfaces nearly parallel to the bands observed microscopically. The decrease of the

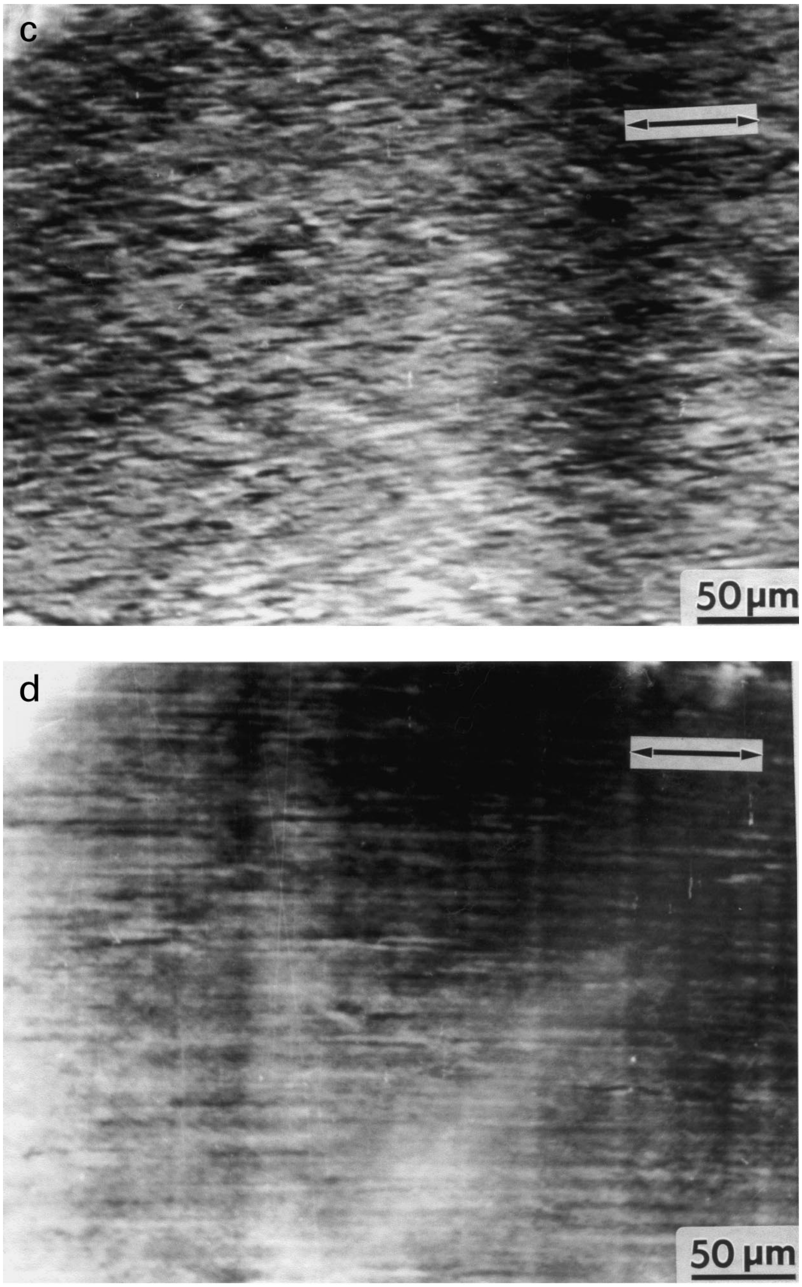

Fig. 8. (*continued*)

long period of these lamellae with increasing strain and continuous rotation of their normals towards loading direction indicate that the deformation mechanism causing the reorientation process was most probably a crystallographic slip along direction of the chain. That slip should result in rotation of chain axis toward flow direction accompanied by rotation of lamella normals towards loading direction [2]. It should also lead to thinning of sheared lamellae, hence to the decrease of the long period. The changes observed in experimental SAXS patterns agree with the above prediction.

It may be anticipated that further action of such slip mode would produce additional reorientation of the lamellae up to the ultimate orientation of their surfaces parallel to the flow direction. At that deformation stage the 4-point pattern in CD-view might be expected to transform into a 2-point pattern with the maxima located along LD. Concurrently, however, the same active chain slip system should cause further rotation of direction of chain axes towards the flow direction. Such situation, when ultimately both chain axis and lamella surface are oriented along the same direction (here FD) is unrealistic and the discussed slip mechanism must lock in at certain point of the deformation process and then it has to be replaced or supplemented by some other

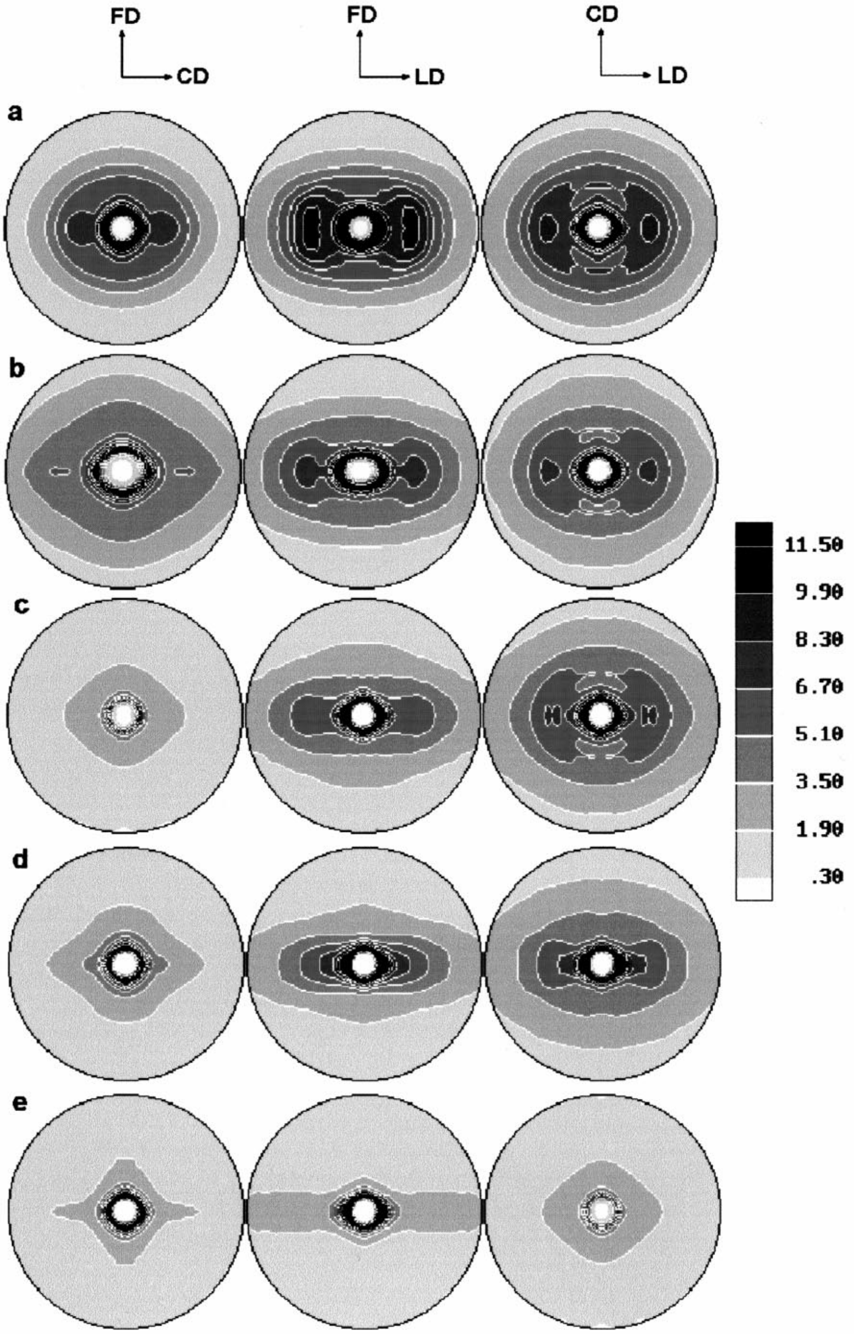

Fig. 9. 2-D SAXS contour plots obtained for the samples deformed to the CR of: (a) 2.1; (b) 3.0; (c) 4.0; (d) 5.7; (e) 6.6. The direction of the incident X-ray beam was along direction of loading (LD, left row), constraint (CD, center row) and flow (FD, right row), respectively.

deformation mechanism in order to accommodate further plastic strain.

New features, supporting above view, appear in the SAXS patterns of samples deformed to higher CR, i.e. 5.7 and further 6.6 (see Figs. 9 and 10). The 2- and 4-point patterns observed for these samples in LD- and CD-views, respectively, transform into diffuse equatorially elongated patterns, with no clear maxima. On the contrary, the scattering pattern observed in the FD-illumination changes much less with increasing strain and retains its 2-point character (albeit with relatively weak maxima) even for CR = 6.6. The intensity of scattering in all patterns, especially these obtained in LD- and CD-illumination modes, is considerably reduced as compared to lower strains. The above changes of the SAXS patterns indicate that the deformation process by slip mechanism was indeed supplemented at the compression above 4.0 by activation of a new deformation mechanism. Since the pattern typical for lamellar organization almost disappears from the experimental SAXS patterns one can expect that the fragmentation of thinned

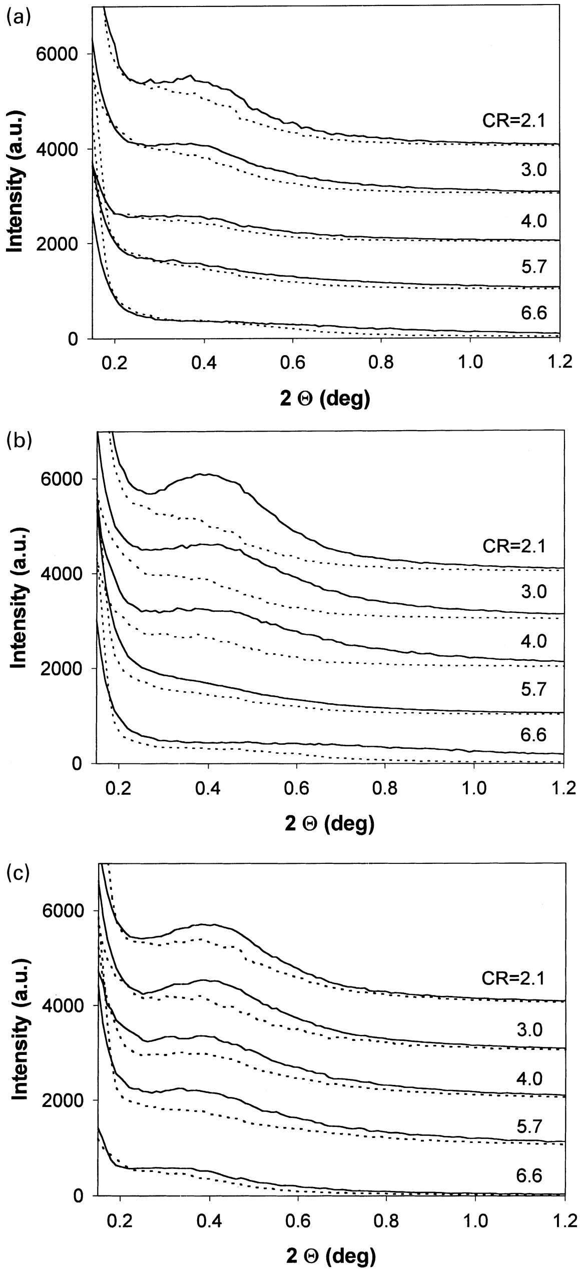

Fig. 10. The sections of the 2-D SAXS patterns of Fig. 9: (a) LD-illumination, sections along CD (solid line) and FD (dotted line); (b) CD-illumination, sections along LD (solid line) and FD (dotted line); (c) FD-illumination, sections along LD (solid line) and CD (dotted line). The CR is indicated for each curve on the plots.

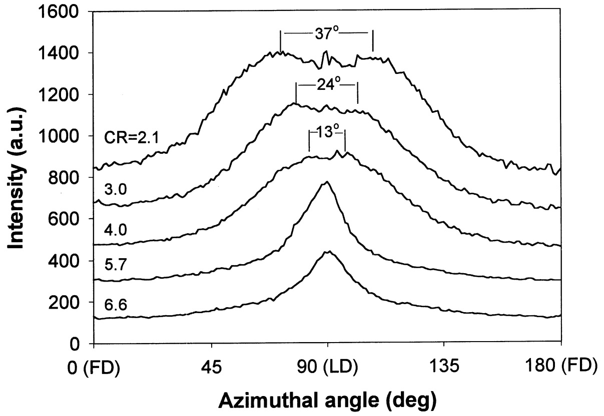

Fig. 11. Scattered intensity distribution vs. azimutal angle obtained from 2-D SAXS CD-view patterns for iPP samples deformed to the CR indicated for each curve. For clarity of presentation the curves were shifted vertically.

lamellae into small blocks occurred at the CR between 4.0 and 5.7. Similar fragmentation was found previously in high density polyethylene deformed by compression in a channel-die at the CR above 3.1 [6]. The patterns recorded for FD illumination demonstrate, however, that a fraction of lamellae, oriented with their surfaces along FD survived and did not undergo fragmentation. The equatorial diffuse streaks present in the LD- and CD-view patterns result probably from scattering by oriented small crystalline blocks formed from the lamellae. After destruction of the lamellae these blocks are distributed much less periodically in space than the parent lamellae and therefore do not produce any clear maximum in the scattering patterns. One can observe merely in the SAXS patterns of samples of CR = 5.7 and 6.6 extremely faint and diffuse maxima which may suggest some periodicity in the range of 10 nm, which is a probable size scale of the newly formed blocks.

3.6. Orientation of crystallites

The evolution of orientation of the crystallites in the compressed samples of iPP was studied by means of X-ray diffraction pole figure technique.

Fig. 12(a)–(d) present the pole figures of the (110), (040), (130), (060) and $(\bar{1}13)$ crystallographic planes of monoclinic iPP crystals (α form), obtained for samples of various CRs.

The diffraction peaks of the (110), (040) and (130) planes frequently overlap with their tails. Moreover, they are superimposed over an amorphous halo and reflections of (021) and $(\bar{1}11)$ crystal planes (Bragg angles 16.2 and 18.2°, respectively). The overlapping of the (040) and (130) peaks is usually much stronger than the overlapping of the (110) and (040) peaks (the difference in position of (040) and (130) peaks is merely 1.6°). The diffraction intensities for pole figure determination were measured using wide receiving slit in order to get values of integral intensities (receiving slit used had usually angular width of 1.3°). As no separation of the contribution of the neighboring overlapping peaks was possible for these data, both (040) and (130) pole figures include some unknown contribution from the other planes, which make these figures less accurate than those measured for non-overlapped peaks. The pole figures obtained for the (110) plane, giving a very strong reflection, are less influenced by the contribution of (021) and (040) planes and by the scattering from the amorphous phase than the (040) or (130) pole figures, but still, there is some level

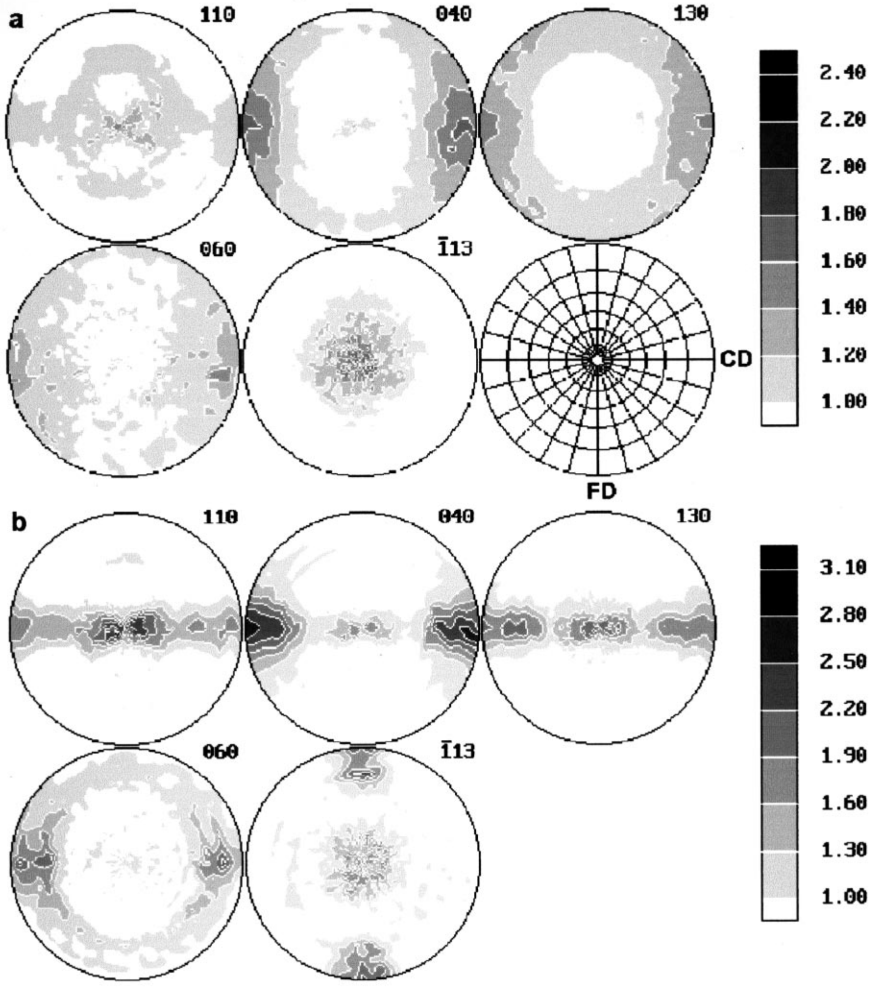

Fig. 12. The pole figures of (110), (040), (130), (060) and ($\bar{1}13$) planes of monoclinic α form iPP for samples compressed in a channel-die to various CRs: (a) CR = 1.54; (b) CR = 3.0; (c) CR = 4.0; and (d) CR = 6.6. All pole figures were plotted in stereographic projection with linear normalized intensity scale. The lower right plot in figure (a) shows the 15° net of polar and azimuthal angles. The flow direction, FD, and constraint direction, CD, are also indicated. Note different scale bars in figures (a)–(d).

of uncertainty. For the reason of limited accuracy of (040) pole figure (which is the most influenced by the other peaks) we measured additionally the pole figure of (060) plane, which in absence of errors should be identical to (040) pole figure. The peak of (060) plane is separated from its neighbors, but unfortunately it has much lower intensity than the (040) peak, thus the accuracy of the pole figure constructed for this plane is also limited. However, the analysis of all mentioned above pole figures together should lead to quite reasonable conclusions.

The pole figures of ($\bar{1}13$) plane were measured since the orientation of this plane is the best possible experimental measure of the orientation of molecular axis in the crystalline phase of iPP sample: the pole of ($\bar{1}13$) plane is located only 5.8° away from direction of molecular axis, equivalent to crystallographic *c* axis.

Fig. 12(a) presents the set of pole figures determined for the sample deformed to CR of 1.54. The poles of (040) and (060) planes cluster around CD for this strain, while the (110) figure shows a weak and diffuse concentration in the equatorial region with a culmination near LD. The (130) pole figure resembles the figures for (0*k*0) planes. No clear preferred orientation of chain axis developed yet (cf. ($\bar{1}13$) figure). The discussed set of pole figures may suggest a relatively weak and diffuse texture of the type of (100)[001] emerging in this sample (the (100)[001] texture is that with (100) planes oriented preferentially perpendicular to LD and chain axis [001] along FD).

Fig. 12(b) illustrates the development of the texture with the CR increasing to 3.0 (we can note that very similar figures to these discussed below were also obtained for sample compressed to CR = 2.4). The main maxima of (040), (060) and (130) remain close to CD. The secondary maxima in (040) and (130) pole figures emerge in the CD–LD equatorial plane, close to LD. Such secondary maxima, however, are not observed in the (060) figure. In the pole figures of (110) plane the maxima are better resolved than for the sample of CR = 1.54. These maxima extend in the

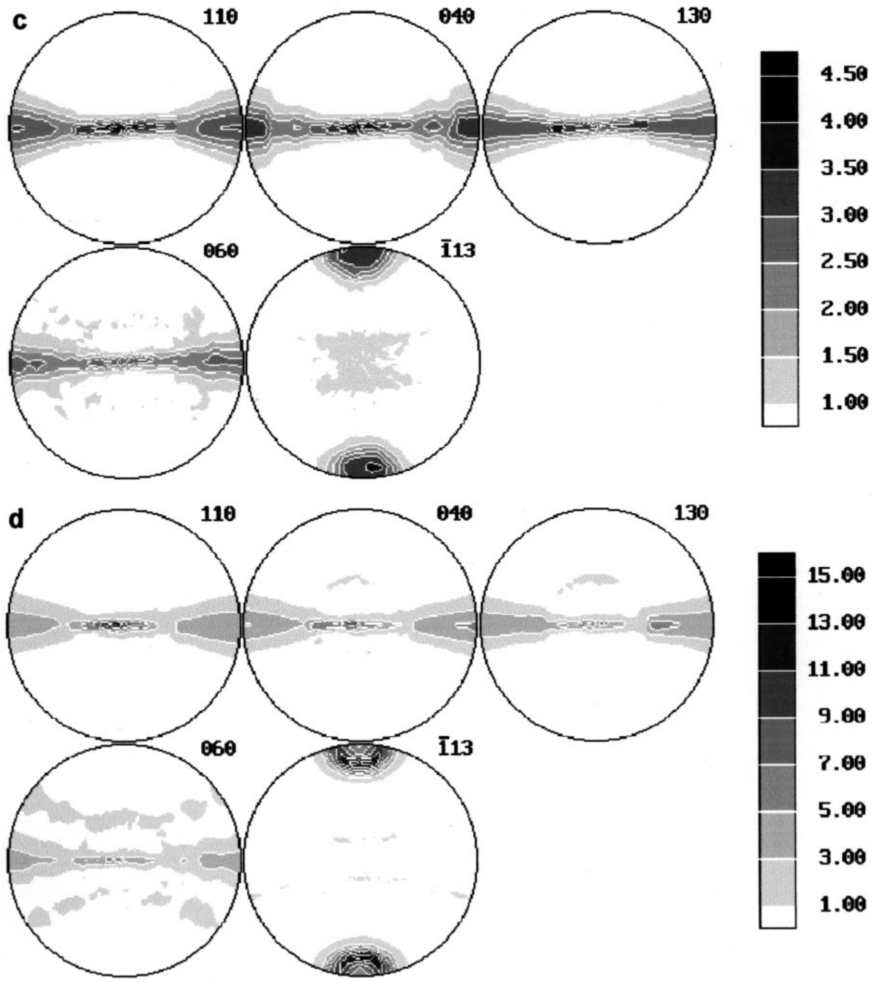

Fig. 12. (*continued*)

equatorial plane from ca. −45 to +45° with respect to LD. Additional, yet weaker, maxima located in the CD–LD plane near CD can be also seen. In the pole figures of the ($\bar{1}13$) plane the maxima around FD can be readily observed. The discussed pole figures suggest that in addition to (100)[001] texture component, present already at lower strain, additional texture components appear and develop for CR of 2.4 and 3.0. These are probably (010)[001] and/or (110)[001]. Since for these compressions the maxima in pole figures remain relatively low (not exceeding 3 m.r.d.) it is difficult to identify unambiguously the components of the texture. For an ideal (010)[001] texture component the maximum of distribution of (040) poles should be observed in LD, while the distribution of (110) poles should have maxima in CD–LD plane, ±72.6° away from LD. The maxima of (130) poles should be placed ±46.8° away from LD. On the other hand, for an ideal (110)[001] texture component the maxima of (040) pole distribution are expected in CD–LD plane ±72.6° away from LD, while the maxima of (110) poles precisely in LD and ±34.8° from LD in CD–LD plane. The poles of (130) planes should concentrate at ±25.8° and ±29.4° away from LD in this equatorial plane.

For CR = 4.0 (see Fig. 12(c)) the intensity at maxima of the pole distributions reach values up to 4.5 times higher than the intensities in a sample of random distribution of orientation. In all (*hk*0) pole figures the maxima of pole distributions are located tightly in the CD–LD plane which, together with the maxima of ($\bar{1}13$) pole figure centered in FD, demonstrate quite sharp orientation of the chain axis in the direction of flow. In the (110) pole figure the main maxima extending near LD are supplemented by maxima of lower intensity, located close to CD. Pole figures of (040) and (060) planes demonstrate similar pattern, although the intensities of the maxima near LD and CD are comparable to each other. The poles of the (130) planes are distributed almost evenly in the CD–LD plane with a broad culmination in the ±45° range around LD. Again, also for this sample all three texture components: (100)[001], (010)[001] and (110)[001] can be expected. The relative high maxima of (110) located in LD may suggest development of the (110)[001] texture component on this deformation stage faster than other components.

With compression increasing to CR = 5.7 and then to 6.6 (see Fig. 12(d)) the texture of the deformed sample sharpens progressively with the maxima rising above 15 m.r.d., but the main features remain similar to the sample of CR = 4.0. The maximum of (110) pole figure in LD is very well developed and sharp, while those near CD are more diffused. In (040) and (060) pole figures the maxima remain close to LD and in regions close to CD (for sample of CR = 5.7, not shown here, these maxima set in approximately ±70° from LD). The pole figure of (130) plane exhibits broad concentrations of poles around LD and additionally from 45° away from LD up to CD in the CD–LD plane. In the figure of the $(\bar{1}13)$ plane the poles concentrate in the 5–10° rings centered around FD with definite maxima located at the intersection of these rings with the FD–LD plane. This clearly demonstrates the orientation of chain axis precisely along FD. However, the overall texture remains multi-component up to the highest CR of 6.6. This texture differs markedly from one-component texture (quasi-single crystal) observed in linear polyethylene deformed in similar conditions [6]. On contrary, it is very close to the texture produced in isotactic polypropylene by uniaxial drawing of wide foils [13]. At high compression the main components of the texture are (110)[001] and (010)[001] components. The (100)[001] orientation developing at initial stages of the plastic deformation (observed at CR = 1.54, cf. Fig. 12(a)) is progressively replaced by those other texture components with increasing strain.

3.7. Deformation mechanisms

The studies of orientation of crystallites revealed that plastic deformation of iPP by plane-strain compression leads to preferred orientation of chain axis of crystallites at relatively early stage of the deformation process. The definite orientation of chain axis along flow direction was detected at the strain as low as 0.87 (CR of 2.4). With increasing strain the respective maxima in pole figures (the poles of $(\bar{1}13)$ plane are the closest to the chain direction; see Fig. 12) continuously develop and sharpen. This indicates increasing number of crystallites approaching that preferred orientation of chain axis parallel to FD with an increase of strain. The SAXS experiments demonstrate that at the same time the lamella normals rotate towards loading direction, while the long period tends to decrease with increasing strain. These observation indicate that the deformation mechanisms active in the deformation process from its early stages are those of the type of crystallographic slip along direction of the chain [001] [2]. At the earliest stages of the plastic deformation this crystallographic slip mechanism must be supported with a deformation of amorphous component by interlamellar slip, which was probably the deformation mode which has been initiated first. The deformation of the amorphous rubbery component is easier to activate than any deformation of crystals, but locks in and ceases at relatively low strain due to large number of tie molecules in amorphous layers and anchored to adjacent lamellae [6]. With increase of strain these tie molecules become soon fully extended and further shear of amorphous layers is almost impossible without disruption of these molecules or fragmentation of the lamellar crystals. The amorphous layers can deform further only to the extent allowed by the progressing deformation of adjacent crystallites.

The first texture component developing in the compressed iPP sample at low strain of 0.43 (CR = 1.54, see Fig. 12(a)) is that with preferred orientation of (100) planes perpendicular to LD while the chain axis tends to orient along FD. Development of such orientation is probably a result of activity of a crystallographic slip operating in (100) plane along chain direction [001], i.e. the (100)[001] slip system. Since the initial orientation of the crystallites in the deformed sample is random, and therefore the conditions for activation of any deformation mechanism are identical, the early initiation of the (100)[001] chain slip demonstrates that this slip is easiest to activate, i.e. has the critical resolved shear stress (CRSS) lower than any other deformation mechanisms. That conclusion is opposite to theoretical considerations [9], which predicted another slip system, (010)[001], as the easiest one. According to that prediction the (100)[001] slip system should be the second, with CRSS higher than of (010)[001]. The same authors noted however, that a specific cross-hatched morphology of spherulitic polypropylene in (α-form can make these slip systems more difficult to activate because the propagation of a particular chain slip in a parent lamella can require activation of more difficult transverse slip in a daughter lamella [9]. Of course, such a coupled slip mechanism would be characterized by higher critical shear stress than for a single slip system. This can be the source of initiation of (100)[001] slip system earlier than others in spite of its supposedly higher critical resolved shear stress.

The pole figures determined for samples deformed to higher strain (above CR = 2.4) demonstrate the development of new texture components: (010)[001] and (110)[001].This indicates that in the discussed strain range the (100)[001] slip system is supplemented by two other chain slip systems of (010)[001] and (110)[001]. These slip systems eventually dominate over the initial (100)[001] chain slip with further strain increase. Such behavior is feasible if we consider that at this strain range the connections between parent and daughter lamellae can be partially destroyed due to proceeding deformation process and these newly activated slip systems can operate independently, not coupled to other mechanisms and then take advantage from their relatively low critical shear stress.

All mentioned above chain slip systems are most probably supported by the transverse slip systems operating in the same planes as chain slips (e.g. (010)[100] transverse slip supporting (010)[001] chain slip) to produce cooperatively the rotations of the crystallites observed in pole figures of deformed samples. Such transverse slip systems had to be active to produce the multi-component texture observed. If only chain slip were active one would expect formation of fiber-like texture with only chain direction aligned along FD and no preferred orientation of (*hk*0) crystallographic planes [2].

The intense shear of the lamellar crystals by chain slip systems produce rotation of chain axis towards FD, while lamellar normals in opposite direction, towards LD. The unlimited activity of such mechanism leads eventually to the unrealistic situation when chain axis aligns nearly parallel to the surface of lamella. We have previously found for high density polyethylene deformed in similar conditions [6] that before that could happen some instabilities of the chain slips proceeding in already thinned lamellae cause their fragmentation into smaller blocks. Such transformation occurs in polyethylene at the CR above 3.1. SAXS data presented in the previous section indicate that similar transformation takes place also during plastic deformation of polypropylene. The scattering characteristic for lamellar structure disappears from the SAXS patterns above the CR of 4.0. This may indicate the destruction of the lamellar structure in this range of the strain. The small crystalline blocks produced by the fragmentation of lamellae as well as adjacent amorphous layers become less constrained than the lamellar structure before fragmentation. This allows further deformation of amorphous component, some rotations of the crystalline blocks and further propagation of active slip systems [6]. These lead to further development of the molecular orientation within the sample with increasing plastic strain. In polyethylene such rotations caused reorientation of crystallites, resulting in reconstitution of a long period perpendicularly to LD at high strain (CR above 6). We did not observe such reconstitution here, in the data obtained for polypropylene. However, the destruction of lamellar structure happens in polypropylene at CR higher than in polyethylene (above 4 vs. 3.1 for HDPE), so it cannot be excluded that similar reconstruction of long period may happen in large-strain plastic deformation of polypropylene at compressions higher than investigated in this study.

The final texture of crystallites in channel-die compressed polypropylene as probed for the plastic strain of 1.89 ($\mathrm{CR} = 6.6$) is a quite complicated multi-component texture. All identified components have a common sharp orientation of chain axis [001] along FD. Two main components dominating the texture of the sample of $\mathrm{CR} = 6.6$ were identified as (010)[001] and (110)[001]. That multi-component texture is opposite to other semi-crystalline polymers deformed in the same deformation mode as high density polyethylene [6] or nylon-6 [32], where one-component textures were observed. On the other hand, the crystalline texture of compressed polypropylene is similar to the texture produced in that polymer by uniaxial foil-drawing at high temperature [13]. In uniaxially drawn samples however, the new long period along machine direction can be easily identified (the machine direction in drawing corresponds to the flow direction in plane-strain compression) while, as discussed above, that new long period does not appear in compressed samples. The identified deformation mechanism active in polypropylene during drawing were (010)[001], (100)[001] and (110)[001] slip systems, i.e. the same as identified here for plane-strain compression, but additionally the {110} twinning modes. There is no evidence of twinning in compression of polypropylene reported in this study.

4. Conclusions

The plane-strain compression of bulk polypropylene in a channel-die produces an oriented material with well developed orientation of chain axis. The texture of that material is multi-component with two main components identified as (010)[001] and (110)[001]. The principal deformation mechanisms active in the deformation process were identified as crystallographic slip systems of (010)[001] (100)[001] and (110)[001] all propagating along chain direction. These slip systems are probably supported by other slip systems acting in the same planes in direction transverse to the chain direction and by interlamellar shear of the amorphous component. The same mechanism were found active in uniaxial drawing of polypropylene. In contrast to deformation by uniaxial drawing no evidence of twinning was found.

The most intense slip modes are (010)[001] and (110)[001]. According to theoretical prediction (010)[001] slip system has the lowest critical shear stress. However, in the course of the plastic deformation in a channel-die the (100)[001] slip system is activated earlier than any other slip system, at low strain. This is probable due to cross-hatched morphology specific for α-spherulites of isotactic polypropylene, which possibly favors the (100)[001] slip system of slightly higher critical shear stress on the initial stages of the deformation process. Later, when that specific morphology is at least partially destroyed the easier (010)[001] and (110)[001] slip systems become to dominate the deformation process.

The intense deformation by crystallographic slip systems leads to a progressive thinning of lamellae and then to their fragmentation and destruction of the entire lamellar structure at the strain above 1.39 ($\mathrm{CR} > 4.0$). The fragmentation is most probably caused by instabilities of the chain slip in already thinned lamellae. Due to compressive forces the lamellar fragmentation is not accompanied with large-scale cavitation of deformed polymer, frequently observed on drawing. The fragmentation of lamellae allows further improvement of chain axis orientation due to rotations of crystalline blocks and their further deformation by crystallographic mechanisms as well as shear of amorphous component. However, no reconstruction of the long period in the direction of flow was found up to the true strain of 1.89 ($\mathrm{CR} = 6.6$).

The morphological alterations on higher levels of hierarchical structure of polypropylene include deformation of spherulites and formation of shear bands within which intense deformation of lamellar crystals is concentrated. The position of the shear bands is not correlated with the boundaries between spherulites. The development and multiplication of these bands leads eventually to the destruction of the initial spherulitic morphology of the sample at relative low plastic strain around 1.1 (CR $\approx$ 3).

Acknowledgements

This research has been sponsored by the State Committee for Scientific Research (Poland) through the grant 7S20401306. SAXS measurements were carried out by M.P. at the Max-Planck-Institut für Polymerforschung, Mainz (Germany) in Prof. T. Pakula research group and were made possible by DAAD Fellowship.

References

[1] Ward IM, Hadley DW. Mechanical properties of solid polymers, New York: Wiley, 1993.
[2] Bowden PB, Young RJ. J Mater Sci 1974;9:2034.
[3] Haudin JM. In: Escaig B, G'Sell C, editors. Plastic deformation of amorphous and semi-crystalline materials, Paris: Les Editions de Physique, 1982. pp. 291.
[4] Lin L, Argon AS. J Mater Sci 1994;29:294.
[5] Peterlin A. Polym Engng Sci 1977;17:183.
[6] Galeski A, Bartczak Z, Argon AS, Cohen RE. Macromolecules 1992;25:5705.
[7] Bartczak Z, Argon AS, Cohen RE. Macromolecules 1992;25:4692.
[8] Unwin AP, Bower DI, Ward IM. Polymer 1985;26:1605.
[9] Aboulfaraj M, G'Sell C, Ulrich B, Dahoun A. Polymer 1995;36:731.
[10] Stockfleth J, Salamon L, Hinrichsen G. Colloid Polym Sci 1993;271:423.
[11] Uejo H, Hoshino S. J Appl Polym Sci 1970;14:317.
[12] Karacan I, Taraiya AK, Bower DI, Ward IM. Polymer 1993;34:2691.
[13] Bartczak Z, Martuscelli E. Polymer 1997;38:4139.
[14] Saraf RF, Porter RS. Polym Engng Sci 1988;28:842.
[15] Saraf RF. Polymer 1994;35:3927.
[16] Bruce GD, Snetivy D, Weatherly GC, Vancso GJ. Die Angew Makromol Chemie 1993;205:171.
[17] Bruce GD, Snetivy D, Weatherly GC, Vancso GJ. Die Angew Makromol Chemie 1993;205:177.
[18] Osawa S, Porter RS. Polymer 1994;35:540.
[19] Osawa S, Porter RS. Polymer 1994;35:545.
[20] Osawa S, Porter RS. Polymer 1994;35:551.
[21] Lafrance CP, Prud'home RE. Polymer 1994;35:3927.
[22] Hibi S, Niwa T, Kyu T, Lin JS. Polym Engng Sci 1995;35:902.
[23] Hibi S, Niwa T. Mizukami. J Polym Engng Sci 1995;35:911.
[24] Dingra VJ, Spruiell EJ, Clark ES. Polym Engng Sci 1981;21:1963.
[25] Taraiya AK, Richardson A. J Appl Polym Sci 1987;33:2559.
[26] Taraiya AK, Unwin AP, Ward IM. J Polym Sci: Polym Phys Ed 1988;26:817.
[27] Pan SJ, Brown HR, Hiltner A, Baer E. Polym Engng Sci 1986;26:997.
[28] Pan SJ, Tang HI, Hiltner A, Baer E. Polym Engng Sci 1987;27:869.
[29] Tang HI, Hiltner A, Baer E. Polym Engng Sci 1987;27:76.
[30] Lin L, Argon AS. Macromolecules 1992;25:4011.
[31] Alexander LE. X-ray diffraction methods in polymer science, New York: Wiley, 1969.
[32] Galeski A, Argon AS, Cohen RE. Macromolecules 1991;24:3953.
[33] Brandrup J, Immergut EH, editors. Polymer handbook 2nd edn.. New York: Wiley, 1975.
[34] Wunderlich B. Molecular physics: Vol. 3. Crystal melting, New York: Academic Press, 1980.
[35] Crissman JM. J Polym Sci: Polym Phys Ed Part A-2 1969;7:389.
[36] Takayanagi M, Yoshino M, Minami S. J Polym Sci 1962;61:S7.
[37] Boyd RH. Polym Engng Sci 1979;19:1010.
[38] McCrum NG. J Polym Sci, Part C: Polym Lett 1964;2:495.
[39] Wada Y, Hotta YJ. J Polym Sci: Part C 1968;23:583.
[40] Inamura I, Ochiai H, Yanamura H. J Polym Sci: Polym Phys Ed 1974;12:2267.
[41] Pluta M, Kryszewski M. Acta Polymerica 1987;38:42.
[42] Jourdan C, Cavaille JY, Perez J. J Polym Sci: Polym Phys Ed 1989;27:2361.
[43] Bartczak Z, Galeski A, Argon AS, Cohen RE. Polymer 1996;37:2113.